

Iterative supervirtual refraction interferometry

Ola Al-Hagan¹, Sherif M. Hanafy², and Gerard T. Schuster³

ABSTRACT

In refraction tomography, the low signal-to-noise ratio (S/N) can be a major obstacle in picking the first-break arrivals at the far-offset receivers. To increase the S/N, we evaluated iterative supervirtual refraction interferometry (ISVI), which is an extension of the supervirtual refraction interferometry method. In this method, supervirtual traces are computed and then iteratively reused to generate supervirtual traces with a higher S/N. Our empirical results with both synthetic and field data revealed that ISVI can significantly boost up the S/N of far-offset traces. The drawback is that using refraction events from more than one refractor can introduce unacceptable artifacts into the final traveltimes versus offset curve. This problem can be avoided by careful windowing of refraction events.

INTRODUCTION

A large-offset refraction survey is a very effective geophysical tool for imaging the subsurface velocity $v(x, y, z)$ structure within the crust and the top part of the mantle. For surveys with source-receiver offsets of tens of kilometers, the first-arrival traveltimes are picked and inverted to delineate the refracting interfaces in the deep crust and the underlying mantle (Musgrave, 1967; Mooney and Weaver, 1989; Operto and Charvis, 1996; Funck et al., 2008). For engineering and exploration applications, source-receiver offsets out to tens or hundreds of meters can easily reveal the smooth velocity distribution to within a few hundred meters of the surface. The resulting velocity tomogram can be very useful for correcting statics problems in reflection data and for revealing the presence of shallow geological anomalies such as faults. The main obstacle with refraction seismology is that the signal-to-noise ratio (S/N) of the

refraction arrivals rapidly falls off with increasing source-receiver offsets. This often results in unreliable picking of far-offset traveltimes and the consequent unreliability in the deep parts of the velocity tomogram.

To mitigate the above problem, Dong et al. (2006) develop refraction interferometry to increase the S/N of the refraction arrivals. They show that the combination of correlating trace pairs and stacking the resulting correlograms over different shots (see Figure 1a) yields a virtual refraction arrival with an increased S/N of \sqrt{N} , where N is the number of postcritical shots shooting into the same pair of geophones. Their results with both synthetic traces and field data show a significant enhancement of the S/N in noisy first arrivals.

Later, Mikesell et al. (2009) and Nichols et al. (2010) demonstrate that spurious energy associated with refractions can provide information about the subsurface. They form a virtual shot record that suppresses uncorrelated noise and yields a virtual refraction that intercepts zero offset at zero time. Mikesell and van Wijk (2011) show that stacking multiple semblance panels at a single virtual shot location can increase the S/N. King and Curtis (2011) also use the virtual refractions in a marine setting for velocity estimation.

To redatum the virtual source to the surface, Mallinson et al. (2011) convolve raw traces with virtual traces to redatum the virtual sources to their original surface locations. They denote this two-step procedure *supervirtual interferometry*, as depicted in Figure 1. The first step shown is to correlate and stack windowed head-wave arrivals to give the virtual trace in Figure 1a. This virtual trace can be associated with a virtual source on the refractor. The second step is to redatum the virtual source to the surface by convolving the virtual traces with the input traces, as shown in Figure 1b.

The theory of refraction interferometry uses the far-field reciprocity equation of the correlation type to create virtual refractions and enhance the S/N. Figure 1a shows the steps for creating virtual refraction traces. The method of Dong et al. (2006) correlates two traces $g(\mathbf{A}|\mathbf{S})$ and $g(\mathbf{B}|\mathbf{S})$ to get the correlation trace $g(\mathbf{B}|\mathbf{A})$ with

Manuscript received by the Editor 5 June 2013; revised manuscript received 6 December 2013; published online 2 May 2014.

¹King Khalid University, College of Science, Physics Department, Abha, Saudi Arabia. E-mail: olahagan@hotmail.com.

²King Abdullah University of Science and Technology, Division of Physical Science and Engineering, Center for Subsurface Imaging and Fluid Modeling, Thuwal, Saudi Arabia and Cairo University, Geophysics Department, Faculty of Science, Cairo, Egypt. E-mail: sh3m3@yahoo.com.

³King Abdullah University of Science and Technology, Division of Physical Science and Engineering, Center for Subsurface Imaging and Fluid Modeling, Thuwal, Saudi Arabia. E-mail: gerard.schuster@kaust.edu.sa.

© 2014 Society of Exploration Geophysicists. All rights reserved.

the virtual source at subsurface point A' and having an unknown excitation time equal to the negative of the traveltimes from A to A' . Here, S is the source location and A and B are the receiver locations (see Figure 1). Repeating this procedure for any postcritical source locations along the same receiver line will result in a virtual trace with the same virtual refraction traveltimes. Stacking correlated traces $g(B|A, t)$ over all postcritical source locations will result in a trace containing a virtual refraction event with an improved S/N. However, there are several problems with correlated refraction waves. One problem is that the virtual refraction trace has an unknown excitation time when refraction arrivals are correlated with each other (see Figure 1a, in which the virtual trace has a virtual source at receiver location A' with excitation time equal to the negative of the traveltimes from A to A' , a correct excitation time is required to find the depth to the refractor). To remedy this problem, Dong et al. (2006) propose that the virtual source can be relocated to the surface by adjusting the stacked virtual refraction traces to an experimental traveltimes in the raw data. Another problem is that the source-receiver offset of the virtual traces will be decreased because they are associated with shorter raypaths and shorter traveltimes.

To overcome these problems, Mallinson et al. (2011), Bharadwaj et al. (2011), and Hanafy et al. (2011) introduce the theory of supervirtual refraction interferometry (SVI). In their method, the receiver spread can be extended to its maximum recording offset and the arrival time is properly accounted for. This method generates virtual far-offset refraction arrivals by correlating two traces (Figure 1a) and convolving the virtual traces from Figure 1a with the raw traces to produce supervirtual refraction traces as illustrated in Figure 1b. This is similar to the procedure proposed by Dong et al. (2006), except their traveltimes shift from a master trace is replaced by convolution with a recorded trace.

After applying SVI, the first-arrival picks will have a high S/N as a result of attenuating the random noise. The S/N can be increased by a factor of \sqrt{N} where N is the number of contributing sources (Mallinson et al., 2011); hence, if there are not enough postcritical sources, SVI might not provide sufficient noise suppression. To overcome this problem, we now extend SVI to iterative supervirtual refraction interferometry (ISVI) and demonstrate its effectiveness with both synthetic and field data. The key idea is that the virtual refraction traces are reused as input into the interferometry procedure. This has the effect of reinforcing the signal and diminishing

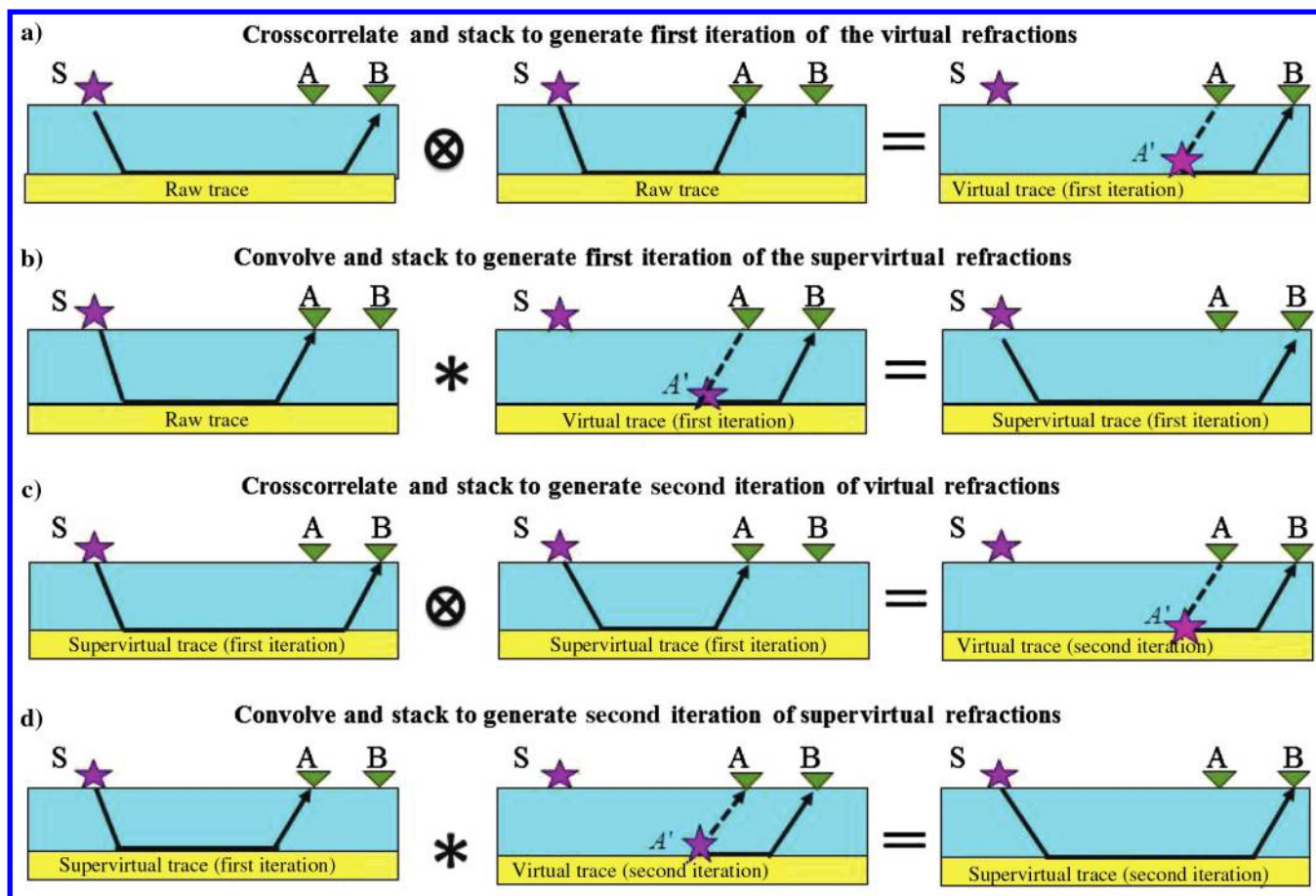


Figure 1. The steps for iteratively creating supervirtual refraction arrivals. (a) Correlation of the recorded trace at A with that at B for a source at S gives the trace $g(B|A)$, followed by stacking over all postcritical source positions. (b) Similar to panel (a) except the virtual refraction traces are convolved with the actual refraction traces and stacked for different geophone positions. (c) Correlation of the first iteration of supervirtual trace at A with that at B for a source at S gives the second iteration of virtual traces; this is followed by stacking these virtual traces over all postcritical source positions. (d) Similar to panel (c) except the second iteration of virtual refraction traces (c) are convolved with the first iteration of the supervirtual traces from (b) to provide the second iteration of supervirtual traces, followed by stacking these new traces for different geophone positions. Here, solid lines represent positive times and dashed lines represent negative times.

noise. Here, the noise suppression is similar to the singular value decomposition method for enhancing Green's function recovery in microseismic data (Melo et al., 2010; Melo and Malcolm, 2011) and in interpolating marine data (Hanafy and Schuster, 2014).

In this paper, the theory of ISVI is presented in the following section and then the results for applying ISVI to both synthetic and field data sets are presented. The Appendix A relates the iterative reconstruction of the refraction waves to the successive substitution method and to the least-squares approach.

THEORY

The far-field reciprocity equations (Schuster, 2009) are used to create supervirtual refractions and enhance the S/N for P-wave refractions (Mallinson et al., 2011; Bharadwaj et al., 2012):

$$\text{Im}[g(\mathbf{B}|\mathbf{A})^v] \approx k \int g(\mathbf{A}|\mathbf{S})^* g(\mathbf{B}|\mathbf{S}) d^2S, \quad (1)$$

$$g(\mathbf{B}|\mathbf{S})^{\text{svi}} \approx 2ik \int g(\mathbf{A}|\mathbf{S}) g(\mathbf{B}|\mathbf{A})^v d^2A, \quad (2)$$

where \mathbf{S} is the source location in Figure 1 and \mathbf{A} and \mathbf{B} are receiver locations; $g(\mathbf{B}|\mathbf{A})^v$ is the virtual trace for a virtual source at \mathbf{A} and a receiver at \mathbf{B} (Figure 1a), where only the refraction arrival is of interest as shown in Figure 1a; the Green's function $g(\mathbf{B}|\mathbf{S})^{\text{svi}}$ represents the supervirtual data obtained by convolving the recorded traces $g(\mathbf{A}|\mathbf{S})$ with the virtual traces $g(\mathbf{B}|\mathbf{A})^v$ (Figure 1b); and k is the average wavenumber.

Windowing around the refraction waves before crosscorrelation is essential to suppress artifacts related to the unintended correlations between reflections, direct arrivals, and refractions. This is similar to the windowing operation done for VSP data (Yu and Schuster, 2004) or seismic data in general (Snieder et al., 2006, 2008). The window is designed to mute all arrivals except those from the same refractor that arrive within about one to two periods of the estimated first-arrival time. The input to SVI is the windowed refraction traces, and the outputs are supervirtual traces with enhanced S/N of the first arrivals.

Unfortunately, the S/N enhancement of SVI is sometimes insufficient for accurate picking of far-offset arrivals. In this case, we now suggest that the SVI traces, called \mathbf{d} , be used as the new input and the output will be far-offset traces with better S/N (Figures c and d). We denote this procedure ISVI, which can be described by the following formula:

$$\mathbf{d}^{(K+1)} = \mathbf{L}[\mathbf{d}^{(K)}], \quad (3)$$

where $\mathbf{L}[\]$ represents the normalized supervirtual interferometry operations of summed correlation and convolution in equations 1 and 2, where $\mathbf{d}^{(0)}$ represents the initial input traces. This means that the input to the SVI operations at $K = 0$ is the raw windowed data $\mathbf{d}^{(0)}$ and the output is the supervirtual data $\mathbf{d}^{(1)}$ obtained by the sequential application of equations 1 and 2. Then, the input to the SVI operations at $K = 1$ is the SVI output $\mathbf{d}^{(1)}$ to produce the $\mathbf{d}^{(2)}$, and this procedure is repeated until acceptable convergence. This iterative method is equivalent to the method of successive substitution for estimating the dominant eigenvector of a matrix. See Appendix A for a detailed description.

The final result is a supervirtual shot gather with the refraction arrivals having a much greater S/N than the original data and the initial supervirtual data. This can effectively widen the aperture of usable refraction data by increasing its quality so that previously unpickable far-offset refractions with poor S/N are now pickable. The potential liability of ISVI is that the wavelet is broadened by the iterative autocorrelation of the source wavelet and that a finite-recording aperture will lead to loss of spatial resolution in the iterated result. The wavelet broadening problem can be alleviated by wavelet deconvolution (see the next section), and resolution loss can be limited by using just a small number of iterations. The degree of smoothing can be estimated by comparing the accurate part of the raw traveltimes to the traveltimes from the final result.

WAVELET DECONVOLUTION

The wavelet spectrum $W(\omega)$, where ω is the frequency, is altered after applying the crosscorrelation and convolution operations. The phase of the supervirtual wavelet is the same after correlation and convolution, but its amplitude spectrum is peakier because the final amplitude spectrum of the wavelet is $|W(\omega)|^3$, the cube of the original. This means that the supervirtual source wavelet is more ringy than the original and can lead to an ambiguous identification of the first arrival. A partial remedy is to pick the first arrival for several near-offset traces from the raw section. Then apply ISVI to the data set, and use these picked traveltimes to correct the traveltimes of the supervirtual traces (Hanafy et al., 2011). Another option is to use a deconvolution filter (Snieder and Safak, 2006; Vasconcelos and Snieder, 2008), which can be applied to the virtual traces to reduce the ringyness in the first arrivals. Here, we created the deconvolution filter by windowing around the first-arrival wavelet. The deconvolution equation is given by

$$D_{\mathbf{BA}} = g(\mathbf{A}|\mathbf{S})g(\mathbf{B}|\mathbf{S})^*/(|g(\mathbf{B}|\mathbf{S})|^2 + \epsilon), \quad (4)$$

where ϵ is a small positive number to avoid instability, $g(\mathbf{A}|\mathbf{S})$ is the data for shot \mathbf{S} and receiver \mathbf{A} , and $g(\mathbf{B}|\mathbf{S})$ represents the data for shot \mathbf{S} and receiver \mathbf{B} (see Figure 1). The effect of equation 4 is to sharpen the wavelet in the crosscorrelation so that the ISVI wavelet after convolution is similar to the original wavelet.

The flowchart in Figure 2 depicts the processing steps for iteratively computing supervirtual traces, and the details are described below:

- 1) Window around the first arrivals in each shot gather, where the suggested window length is two to three periods before and after the expected first-arrival times. Also, mute the near offsets to eliminate the direct-wave and to isolate the refractions from one interface from the other refractions.
- 2) Use equation 1 to generate the virtual traces (see Figure 1a).
- 3) Apply a wavelet deconvolution filter (equation 4) because the source wavelet has broadened due to the correlation of traces with one another.
- 4) Use equation 2 to generate the supervirtual traces (see Figure 1b).
- 5) If the first arrivals are still unpickable, use the output of step 4 as an input and repeat steps 2–4 (see Figure 1c and 1d).
- 6) Repeat step 5 until the first arrivals show a sufficiently large S/N.

In the next section, we will demonstrate the effectiveness of this approach using synthetic data and a field data set from Saudi Arabia.

NUMERICAL RESULTS

Synthetic data example

ISVI is now tested with synthetic data. We simulate a normal fault with a low-velocity colluvial wedge and a local velocity anomaly near the surface (Figure 3). The synthetic shot gathers

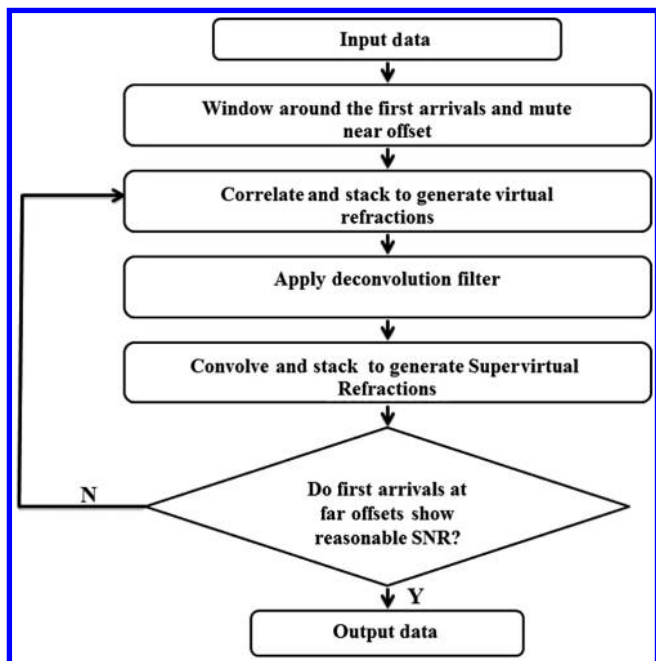


Figure 2. Flowchart for obtaining ISVI traces.

are generated using a finite-difference solution to the 2D acoustic wave equation for a horizontal line of 120 shots with 120 trace per shot gather and a 5 m shot and receiver interval (Figure 4a). The source time history is a Ricker wavelet with a peak frequency of 30 Hz.

Random noise (with a uniform probability distribution and a bandwidth of 10–100 Hz) is added to the traces so that the far-offset refraction arrivals are no longer visible nor pickable. Figure 4b shows a shot gather after adding random noise, and Figure 4c shows the windowed first arrivals, where the window length is three periods centered about the expected first-arrival times. The windowed arrivals need to be only refraction waves from the same refractor. Bharadwaj et al. (2012) suggest examining common-receiver pair correlation gathers (CPGs) to determine if this condition is satisfied by the flattening of correlated refraction arrivals across the gather. For refraction waves, all the postcritical sources are at stationary points for a fixed pair of inline receivers; therefore, correlating the traces for the specified receiver pair will result in flat events in the common correlation-pair gather. Flat events in the common correlation-pair gather correspond to refraction arrivals from a given refractor. However, parallel flat events shifted in time indicate the

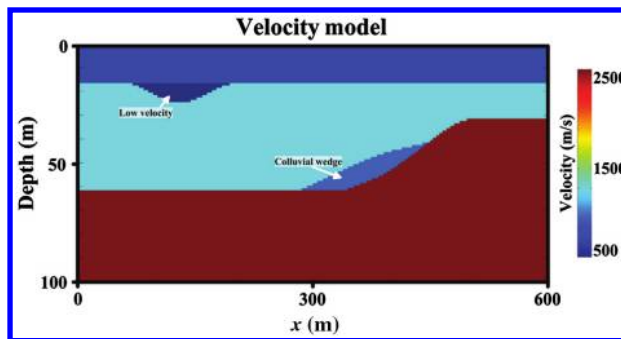
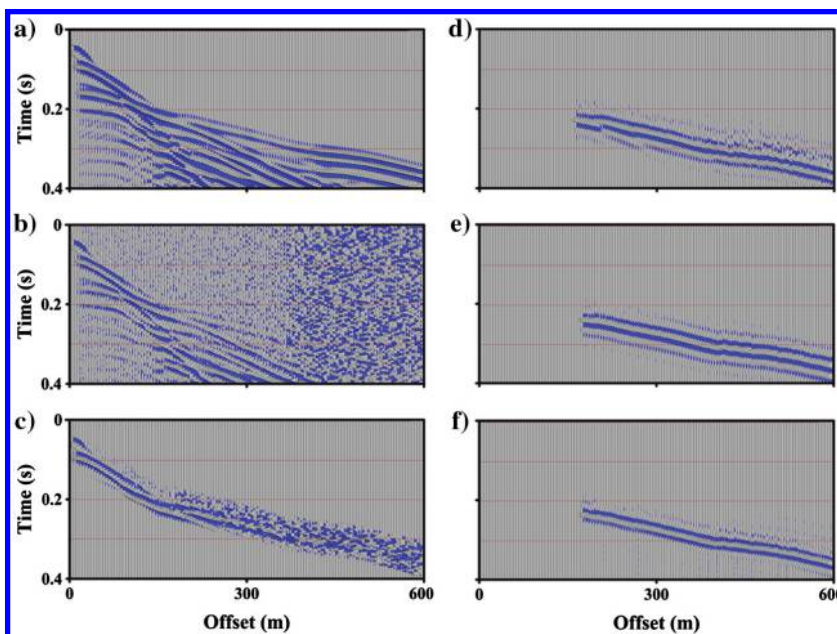


Figure 3. Acoustic velocity model used to generate the synthetic data. This model resembles a cross section of the Qadimah fault.

Figure 4. (a) A synthetic CSG. (b) Same as (a) after adding random noise to mask the first arrivals. (c) Same as (b) after windowing around the first arrivals. (d) The traces after one iteration of ISVI and (e) after the third iteration. (f) Same as (e) except a deconvolution filter is applied to the traces.



existence of several refractors. In this case, arrivals from each refractor should be processed separately.

Figure 4d shows the supervirtual shot gather after one iteration. Here, the S/N of the traces is improved but the far-offset traces are still unpickable. Figure 4e and 4f shows the same traces after three SVI iterations with and without the application of the deconvolution filter, respectively. We notice a dramatic increase in the S/N of the ISVI traces compared to the SVI traces. The previously obscured first-arrival traveltimes are now clearly visible and can be picked.

It is possible to pick all of the first arrivals in the noise-free synthetic data set (up to 600 m); however, after adding random noise, accurately picking the first arrivals can only be achieved up to an offset of 300 m. After applying iterative refraction interferometry, the first arrivals can be picked to an offset of 440 m after the first iteration and 600 m after the third iteration. Thus, ISVI is able to increase the pickable first arrivals from source-receiver offsets of 300 to 600 m. Figure 5 shows histograms of the differences between the traveltimes picks for the ISVI data and the noise-free original synthetic data and shows that most of the events have a traveltimes difference of less than $T/4$, where T is the dominant period of the source wavelet (in this case $T = 33$ ms).

Figure 6 shows the traveltimes picks plotted against the source-receiver offset for three common-shot gathers. In this figure, the picking errors are mostly less than $T/4$. At the near offsets, the red (second iteration) picks and the blue (fourth iterations) picks do not exist because we muted the near-offset data as part of our data processing to reduce the crosstalk noise of reflections and direct waves and enhance the refraction arrivals. The time shift between the green (noise-free raw data) picks and the ISVI picks (red, $K = 2$ and blue, $K = 4$) is caused by the distortion of the source wavelet as well as the interference from other events in the window.

Field data example

A refraction field data set is recorded along the western coast of Saudi Arabia next to a fault system called the Qadimah fault. A total of 120 active receivers are used with receiver offsets of 2 m, and a total of 120 shot gathers are collected with one shot located at each receiver location. The shot is a 12-lb hammer striking a metal plate with dimensions of $15 \times 15 \times 3$ cm. The frequency spectrum of this data set is peaked around 40 Hz; therefore, a band-pass filter with a low-cut linear ramp of 5–10 Hz and a high-pass linear ramp of 100–120 Hz is used to remove low- and high-frequency noise (Figure 7a and 7b). In Figure 7b, the far-offset traces show a low S/N and the first-arrival traveltimes cannot be picked.

A tapered time window with a length of two periods centered around the first-arrival traveltimes is applied to the recorded traces (Figure 7c). From our experience, we found that the shorter the window, the fewer the artifacts in the final results, especially when reflections or refractions from another interface exist near the refraction of interest. CPGs should be used here to ensure the windowed arrivals are refractions that originate from the same refractor (Bharadwaj et al., 2011).

Figure 7c shows that the first arrivals are clearly visible to around source-receiver offset of 120 m offset, but beyond this offset, the

S/N is very low and the first arrivals cannot be picked. The supervirtual traces after one iteration of ISVI are shown in Figure 7d. The first arrivals are clearly visible up to 200 m offset, but beyond this offset, the S/N remains low and the first arrivals cannot be picked. Figure 7e shows the traces after the third iteration, where the S/N of the traces has dramatically increased. The previously masked first-break refracted arrivals are now clearly visible and easy to pick. Because the supervirtual source wavelet can lead to an ambiguous identification of the first arrival, we apply a deconvolution filter (equation 4) to the virtual traces, which reduces the ringiness in the first arrivals as observed in Figure 7f.

Figure 8 shows the histograms of the differences between the traveltimes picks for both the ISVI second iteration picks and the raw picks, and it shows that most of the events have a traveltimes difference of less than $T/4$ (here $T = 25$ ms). To demonstrate the importance of accurate first-arrival picks at the far offsets, the velocity tomogram (Buddensiek et al., 2008) computed from the first-arrival traveltimes of the bandpass-filtered data (Figure 7b) are shown in Figure 9. The total number of recorded traveltimes is 14,400. To eliminate unreliable picks, a reciprocity test, where the traveltimes from the source at A to a receiver at B should be equal to the traveltimes from the source at B to a receiver at A (Sheriff, 2002),

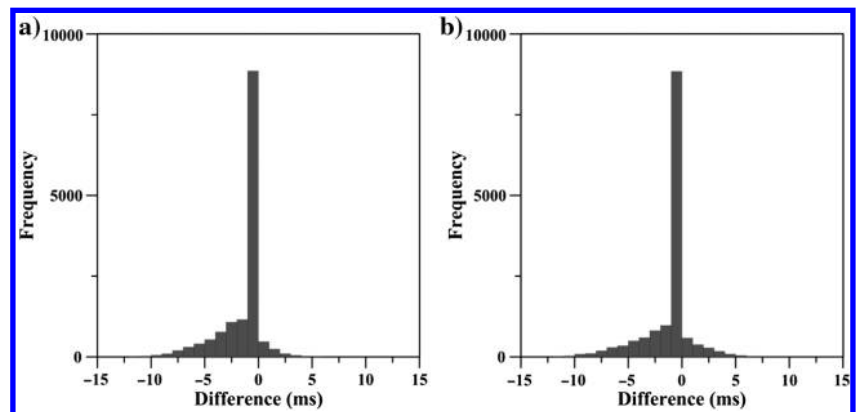


Figure 5. Histogram of traveltimes difference between the first-arrival traveltimes picks in the synthetic data and the iterative supervirtual data after the (a) second and (b) fourth iterations.

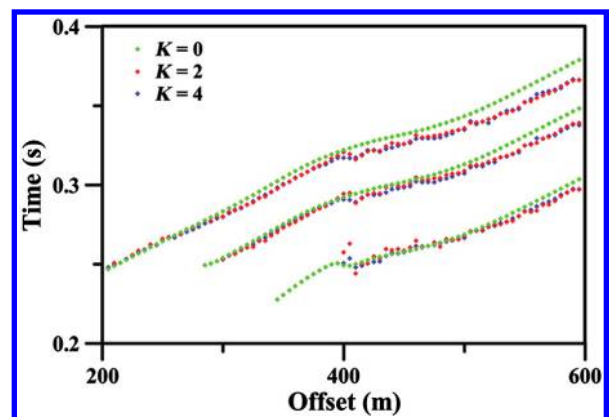


Figure 6. Comparison between the picked traveltimes for the raw traces and the ISVI traces after two and four iterations for shot gathers 1, 40, and 60 located at 5, 200, and 300 m, respectively.

is carried out so that only 11,024 accurate picks are included in the inversion with a maximum source-receiver offset of 116 m. All eliminated picks are from far-offset receivers. The first-arrival traveltimes of the ISVI data set are also picked and are inverted (Figure 10). In this case, 13,524 picks passed the reciprocity test with a maximum source-receiver offset of 238 m. Most of the extra traveltimes picks are those from far offsets that show a low S/N in the raw data set. To invert both data sets, we started with the same initial velocity model, which is a model characterized by a gradually in-

creasing velocity with depth. Here, the velocity starts at 300 m/s at the top and gradually increases to 3000 m/s at 60 m depth. The numbers of pixels in the model (the unknown) are equal to or less than one-third of the number of picks used in the inversion. A total of 40 iterations are applied to get the final tomograms, and then a masking filter is applied to the final tomogram to remove velocity values at pixels not intersected by a ray. The final tomograms are shown in Figures 9 and 10, where the depth of the ISVI tomogram is almost doubled compared to the SVI tomogram.

SANITY CHECK

Can the ISVI method distort the arrival times of the first arrivals? To answer this question, we generated synthetics for two velocity models. The first is a two-layer velocity model (Figure 11a), in which the bumpy refractor induces bumps in the refraction profile. The second velocity model is a three-layer model (Figure 11b), in which the first refractor is identical to that of the two-layer velocity model and a second horizontal refractor is added to the bottom part of the model. The traveltimes are calculated using a finite-difference solution to the eikonal equation (Qin et al., 1992), and the common shot gathers (CSGs) are then generated using traces that contain a 100 Hz Ricker wavelet that begins at the calculated traveltimes of that trace. This procedure generates a noise-free data set that only contains head waves. Traces corresponding to direct wave events are muted from all shot gathers.

Three synthetic experiments are conducted to examine the ISVI capability as follows:

- 1) Using the two-layer velocity model and noise-free data set, the noise-free CSGs are input for 10 ISVI iterations. The first-arrival traveltimes for the raw data and each of the 10 iterations ISVI are picked and plotted in Figure 12a. The first-arrival traveltimes after 10 ISVI iterations are almost identical to the traveltimes of the raw data with an error of \pm one sample, which can be due to human-picking accuracy.
- 2) Using the two-layer velocity model and noisy data set, we added white noise to the CSGs and repeated the 10 ISVI

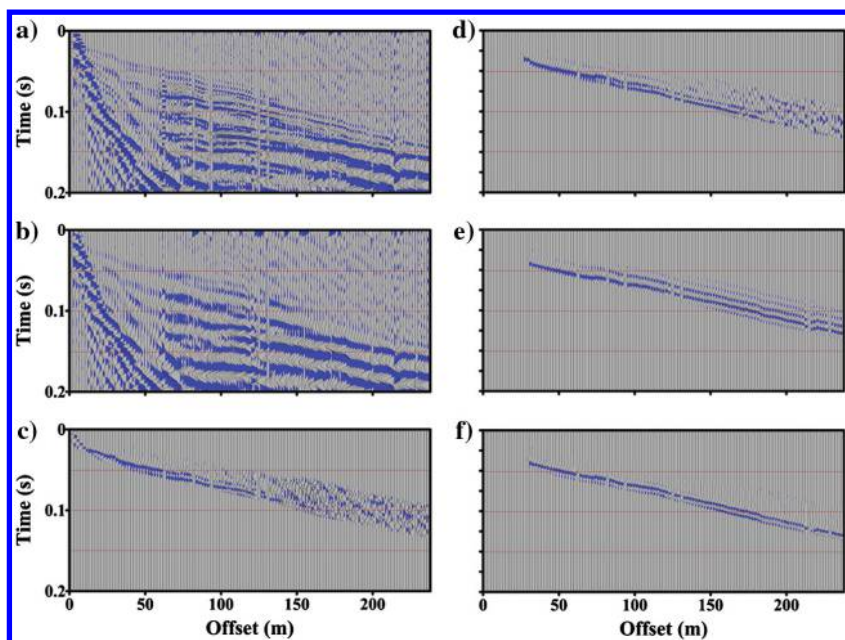


Figure 7. (a) Raw CSG. (b) Same as (a) after band-pass filtering. (c) Same as (b) except muting around the first arrivals. (d) The traces after the first iteration of SVI. (e) The traces after the third iteration. (f) Same as (e) except a deconvolution filter is applied to the traces.

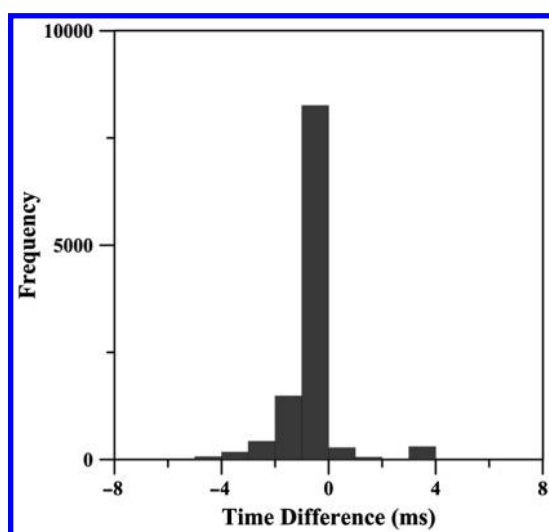


Figure 8. Histogram of traveltime difference between the first-arrival traveltimes in the raw data and those obtained from the ISVI second iteration for the field data.

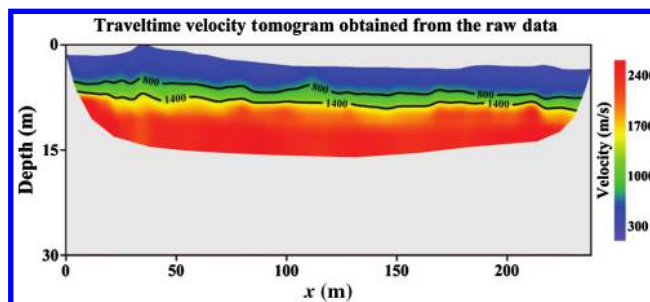


Figure 9. Velocity tomogram obtained by inverting the first-arrival traveltimes in the raw data. The black lines represents the contour lines at 800 and 1400 m/s, which represent the expected location of the first and second refractors.

iterations. The first-arrival traveltimes after each iteration are picked and plotted in Figure 12b. The first-arrival traveltimes for the 10 iterations are almost identical to that of the raw data, and the error between the ISVI and raw picks is very small (± 3 samples).

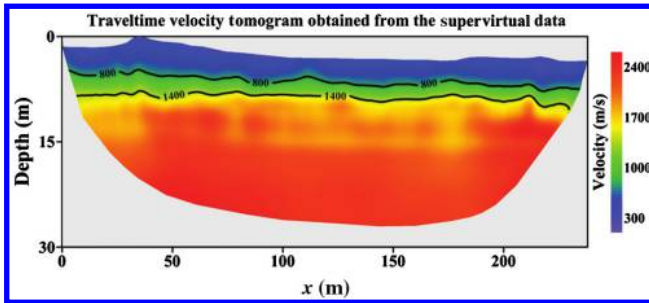


Figure 10. Velocity tomogram obtained by inverting the first-arrival traveltimes in the ISVI data. The black lines represent the contour lines at 800 and 1400 m/s, which represent the expected location of the first and second refractors.

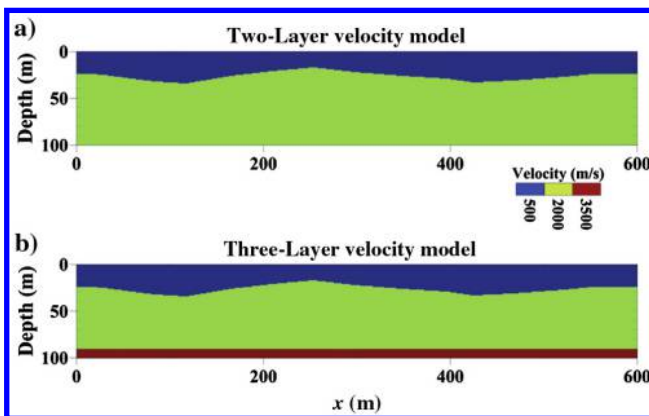


Figure 11. The (a) two- and (b) three-layer velocity models used for the sanity check test.

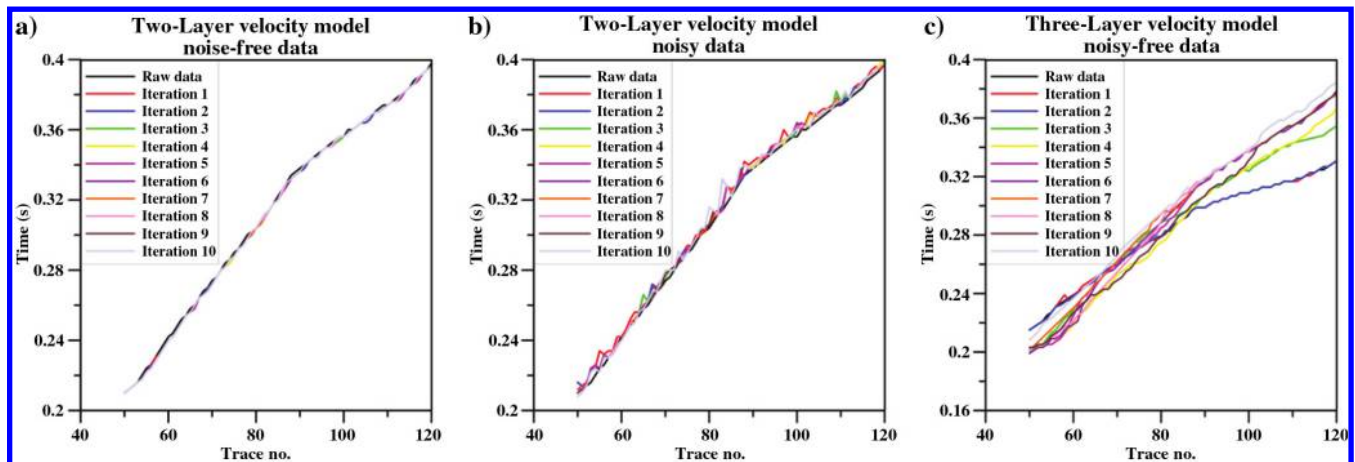


Figure 12. The traveltimes picks of the sanity check test. (a) Two-layer model with noise-free data, (b) two-layer model with noise added to the data, and (c) three-layer model with noise-free data.

- 3) The three-layer velocity model used to generate the input CSGs following the procedure described earlier. In this test, we muted the direct arrivals and retained arrivals from both the first and second refractors. After 10 ISVI iterations, the picked traveltimes show large errors (up to 27 samples), especially at the long offsets. Picked traveltimes after the first and second iterations are similar, but then traveltimes errors increase with increasing iteration number and offset. A closer look at the ISVI picks shows that the bumps in the raw data are gradually smoothed out with increasing the number of iterations.

This result says that the refraction arrivals from one interface must be isolated from the others by careful windowing. Otherwise, the distortion of ISVI traveltimes will grow with increasing offset and iteration number.

CONCLUSIONS

We presented the theory of ISVI for increasing the offset range of pickable first arrivals. The assumptions are that the first arrivals are refraction waves from the same layer. Our synthetic data suggest that the offsets of pickable first arrivals in ISVI traces can be more than doubled compared to the noisy raw data. The application of ISVI to a Saudi refraction survey shows that more 22% traveltimes could be picked at the far offsets after three iterations compared to the raw data. This increases the image depth to more than 40%. Finally, CPGs should be used to ensure the windowed arrivals are from the same refractor, and ISVI traveltimes should be compared to the raw traveltimes to detect excessive smoothing of the ISVI traveltimes.

ACKNOWLEDGMENTS

We thank the 2011–2012 sponsors of the CSIM Consortium (csim.kaust.edu.sa) for their support. We also thank KSL, King Abdullah University of Science and Technology, for the use of the Shaheen supercomputer.

APPENDIX A

RECONSTRUCTION OF REFRACTION WAVES
BY SUCCESSIVE SUBSTITUTION METHOD

We now show that the ISVI procedure is equivalent to the method of successive substitution for estimating the dominant eigenvector of a matrix. More generally, ISVI is related to a fixed-point method for finding the fixed point of a mapping operator (Shashkin, 1991).

Define $g(\mathbf{B}, t|\mathbf{A}, 0)$ as a noisy refraction trace (see Figure A-1) recorded at \mathbf{B} and generated by a band-limited 2D point source, where a 2D point source is a line source in 3D, at \mathbf{A} with excitation time equal to zero. The recording time is t , and only the refraction arrival is recorded. The virtual trace $g(\mathbf{B}, t|\mathbf{A}, 0)^{\text{virt}}$ generated by the reciprocity theorem of correlation type (Wapenaar and Fokkema, 2006) in the far-field approximation is given by

$$g(\mathbf{B}, t|\mathbf{A}, 0)^{\text{virt}} = \int_{X_f} \dot{g}(\mathbf{A}, t|\mathbf{x}, 0) \otimes g(\mathbf{B}, t|\mathbf{x}, 0) dx; \quad \mathbf{A}, \mathbf{B} \in X_r, \quad (\text{A-1})$$

where the receiver is at \mathbf{B} and the velocity c is set equal to 1 for convenience. The dot indicates the time derivative, and \otimes defines the one-sided crosscorrelation operation in time with lag times ≥ 0 . A horizontal source line at $z = 0$ is assumed to be near the free surface with source points $\mathbf{x} = (x, 0) \in X_f$, and the integration is over the postcritical source offset points $\mathbf{x} \in X_f$. Receiver positions $\mathbf{B}, \mathbf{A} \in X_r$ are also a horizontal line just below the source line and belong to the receiver and are denoted by the set of receiver locations X_r . For convenience, a horizontal refractor is assumed to be at depth $z = l$, where the receivers are located at $\mathbf{A} = (A, l)$ (see Figure A-1). The goal is to estimate the optimal $g(\mathbf{B}, t|\mathbf{x}, 0)$ that is free of interfering coherent and random noise.

Dong et al. (2006) interpret equation A-1 as a refraction trace with a virtual source located on the refractor with an unknown excitation time; this is sometimes known as datuming a source to depth. To *dedatum* the source (Bharadwaj et al., 2011; Mallinson et al., 2011) back to the surface, we apply the far-field convolution theorem to the original data and the virtual trace, where $\mathbf{y} = (y, 0) \in X_f$ are also source points:

$$g(\mathbf{B}, t|\mathbf{y}, 0) = 2 \int_{X_r} \dot{g}(\mathbf{y}, t|\mathbf{A}, 0) \star g(\mathbf{B}, t|\mathbf{A}, 0)^{\text{virt}} d\mathbf{A}; \quad \mathbf{B} \in X_r; \mathbf{y} \in X_f. \quad (\text{A-2})$$

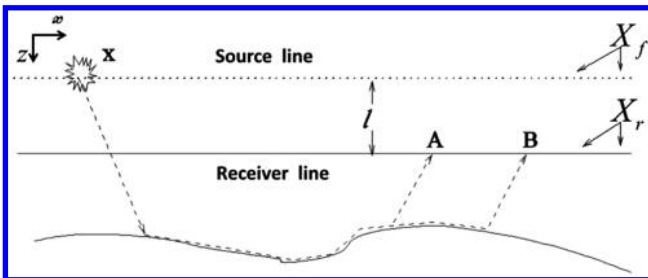


Figure A-1. Velocity model with arbitrary refractor and horizontal source and receiver lines, with the receivers $(A, -l)$ and $(B, -l) \in X_r$ and the sources $(x, 0) \in X_f$ near the free surface.

Substituting equation A-1 into equation A-2 yields

$$\begin{aligned} g(\mathbf{B}, t|\mathbf{y}, 0) &= 2 \int_{X_r} \dot{g}(\mathbf{y}, t|\mathbf{A}, 0) \star \left[\int_{X_f} \dot{g}(\mathbf{A}, t|\mathbf{x}, 0) \right. \\ &\quad \left. \otimes g(\mathbf{B}, t|\mathbf{x}, 0) dx \right] d\mathbf{A}, \\ &= 2 \int_{X_f} \left[\int_{X_r} \dot{g}(\mathbf{y}, t|\mathbf{A}, 0) \star \dot{g}(\mathbf{A}, t|\mathbf{x}, 0) d\mathbf{A} \right] \\ &\quad \otimes g(\mathbf{B}, t|\mathbf{x}, 0) dx, \quad \mathbf{B} \in X_r; \mathbf{y} \in X_f, \quad (\text{A-3}) \end{aligned}$$

where the last equation follows by interchanging the order of integrations and invoking the associative property of convolution and correlation; here, \star denotes temporal convolution.

Substituting

$$L(y, x, t) \doteq 2 \int_{X_r} \dot{g}(\mathbf{y}, t|\mathbf{A}, 0) \star \dot{g}(\mathbf{A}, t|\mathbf{x}, 0) d\mathbf{A}; \quad \mathbf{y}, \mathbf{x} \in X_f \quad (\text{A-4})$$

and

$$d(B, x, t) \doteq g(\mathbf{B}, t|\mathbf{x}, 0); \quad d(B, y, t) \doteq g(\mathbf{B}, t|\mathbf{y}, 0), \quad (\text{A-5})$$

into equation A-3, discretizing the spatial and temporal variables over evenly sampled grids, and approximating the integrations by Riemann sums gives

$$d(B, y, t) = \sum_{x, \tau} L(y, x, t + \tau) d(B, x, \tau) \Delta\tau \Delta x; \quad \mathbf{y} \in X_f; \mathbf{B} \in X_r, \quad (\text{A-6})$$

where $\Delta\tau$ and Δx represent the temporal and spatial sampling intervals and the summations are over the allowed postcritical source positions x and the allowed time samples in the one-sided crosscorrelation function.

Using integer subscripts to denote the evenly sampled space and time samples, the data $d(B, x, \tau)$ become $d(B, x_{j'}, \tau_{j''})$. If each unique combination of indices (j', j'') is mapped onto a unique integer j , then the functions on the right side of equation A-6 can be represented as

$$\begin{aligned} d(B, x_{j'}, \tau_{j''}) &\rightarrow d_j; \\ L(y_{i'}, x_{j'}, t_{i''} + \tau_{j''}) d(B, x_{j'}, \tau_{j''}) \Delta\tau \Delta x &\rightarrow L_{ij} d_j; \quad (\text{A-7}) \end{aligned}$$

and the left side is

$$d(B, y_{i'}, t_{i''}) \rightarrow d_i. \quad (\text{A-8})$$

Substituting equations A-7 and A-8 into equation A-6 gives

$$d_i = \sum_j L_{ij} d_j \quad \text{or} \quad \mathbf{d} = \mathbf{Ld}, \quad (\text{A-9})$$

where the summation is over the allowable source-receiver pairs and time samples that depend on the source and receiver points.

Equation A-9 represents a nonlinear set of equations because, according to equation A-4, the matrix elements L_{ij} depend on d_j . Finding the solution to equation A-9 is equivalent to finding the eigenvector of the \mathbf{L} matrix with the eigenvalue equal to 1. It is also a fixed point mapping of \mathbf{d} back into itself, and conditions for finding this fixed point are described in Shashkin (1991).

It can be argued that if the traces are windowed roughly about the first arrivals, then the refraction wave energy is the dominant energy that satisfies equation A-3 for all postcritical offsets. These windowed first arrivals can be expressed as a weighted sum of eigenvectors

$$\mathbf{d}^{\text{window}} = \sum_i \alpha_i \mathbf{d}_i, \quad (\text{A-10})$$

where \mathbf{d}_i is the i th eigenvector of \mathbf{L} , α_i is the scalar coefficient of the i th eigenvector, and the eigenvectors $(\mathbf{d}_1, \mathbf{d}_2, \dots)$ are arranged in order of decreasing magnitude of their eigenvalues λ_i . All other extraneous arrivals such as reflections and incoherent noise do not satisfy equation A-9 for all postcritical offsets, and so they are not eigenvectors of \mathbf{L} . Hence, the dominant normalized eigenvector \mathbf{d}_1 of equation A-3 should be the refraction wave arrival, which can be found by successive substitution, as shown below.

Estimating the refraction trace by successive substitution: In the following analysis, we will assume that the equations have been normalized so the dominant normalized eigenvector \mathbf{d}_1 has the eigenvalue $\lambda_1 = 1$ and is associated with refraction wave arrivals, $\lambda_1 > |\lambda_i|$ for $i \neq 1$, and $\lambda_i \geq \lambda_{i-1}$ for all $i > 1$. In this case, the starting estimate for $\mathbf{d}^{(0)} = \mathbf{d}^{(\text{window})} = \sum_i \alpha_i \mathbf{d}_i$ can be substituted into equation A-9 to give the first iterate estimate:

$$\mathbf{d}^{(1)} = \mathbf{L}\mathbf{d}^{(0)}, = \sum_i \alpha_i \mathbf{L}\mathbf{d}_i, = \sum_i \alpha_i \lambda_i \mathbf{d}_i, \quad (\text{A-11})$$

Successively substituting each iterate into the right side of equation A-9 gives the K th iterate:

$$\mathbf{d}^{(K)} = \sum_i \alpha_i \lambda_i^K \mathbf{d}_i, = \alpha_1 \lambda_1^K \mathbf{d}_1 + O(\lambda_2^K), \sim \alpha_1 \mathbf{d}_1, \quad (\text{A-12})$$

which is proportional to the eigenvector associated with the refraction wave arrivals. This is exactly the procedure used in the SVI method, except a wavelet deconvolution is sometimes used after each iteration.

Estimating the refraction trace by least squares: An alternative approach to estimate the refraction trace is the least-squares solution of equation A-2 that minimizes the misfit function

$$\epsilon = 1/2(\bar{\mathcal{L}}\bar{\mathbf{d}}_v - \bar{\mathbf{d}})(\mathcal{L}\mathbf{d}_v - \mathbf{d}), \quad (\text{A-13})$$

where the bar indicates the conjugate transpose operation, \mathbf{d}_v is the virtual refraction arrival we seek. Here, \mathbf{d}_v is $g(\mathbf{B}, t|\mathbf{A}, 0)^{\text{virt.}}$, \mathcal{L} is the discretized convolution operator in equation A-2, and \mathbf{d} is the recorded data after windowing about the first arrival (\mathbf{d} is $g(\mathbf{y}, t|\mathbf{A}, 0)$ in equation A-2). The goal is to find the optimal \mathbf{d}_v that minimizes this misfit function.

The misfit gradient is

$$\nabla \epsilon = \bar{\mathcal{L}}(\mathcal{L}\mathbf{d}_v - \mathbf{d}), \quad (\text{A-14})$$

so that the nonlinear steepest descent solution is given as

$$\mathbf{d}_v^{(k+1)} = \mathbf{d}_v^{(k)} - \alpha \bar{\mathcal{L}}^{(k)}(\mathcal{L}^{(k)}\mathbf{d}_v^{(k)} - \mathbf{d}), \quad (\text{A-15})$$

where k denotes the iteration index and α is the step length. Here, we see that the optimal \mathbf{d}_v is found by an iterative sequence of correlation and convolution operations, similar to that for the successive substitution method. The main difference is that the least-squares method updates the solution by using the data residual, which is the difference between the predicted data $\mathcal{L}^{(k)}\mathbf{d}_v^{(k)}$ and observed data \mathbf{d} . The advantage of least squares is that it automatically accounts for source wavelet effects and artifacts due to a finite aperture of sources and receivers and stop at the correct k iteration before too much smoothing occurs. The possible disadvantage is that it might try to predict coherent noise in the data that is not a refraction wave arrival.

REFERENCES

- Bharadwaj, P., G. T. Schuster, W. Dai, and I. Mallinson, 2012, Theory of super-virtual refraction interferometry: *Geophysical Journal International*, **188**, 263–273, doi: [10.1111/j.1365-246X.2011.05253.x](https://doi.org/10.1111/j.1365-246X.2011.05253.x).
- Bharadwaj, P., G. T. Schuster, and I. Mallinson, 2011, Super-virtual refraction interferometry: Theory: 81st Annual International Meeting, SEG Expanded Abstracts, 3809–3813.
- Buddensiek, M.-L., J. Sheng, T. Crosby, G. T. Schuster, R. L. Bruhn, and R. He, 2008, Colluvial wedge imaging using traveltimes and waveform tomography along the Wasatch Fault near Mapleton, Utah: *Geophysical Journal International*, **172**, 686–697, doi: [10.1111/j.1365-246X.2007.03667.x](https://doi.org/10.1111/j.1365-246X.2007.03667.x).
- Dong, S., J. Sheng, and G. T. Schuster, 2006, Theory and practice of refraction interferometry: 76th Annual International Meeting, SEG Expanded Abstracts, 3021–3025.
- Funk, T., M. Andersen, J. Neish, and Dahl-Jensen, 2008, A refraction seismic transect from the Faroe Islands to the Hatton-Rockall basin: *Journal of Geophysical Research*, **113**, B12405, doi: [10.1029/2008JB005675](https://doi.org/10.1029/2008JB005675).
- Hanafy, S. M., O. AlHagan, and F. Al-Tawash, 2011, Supervirtual refraction interferometry: Field data example over a colluvial wedge: 81st Annual International Meeting, SEG Expanded Abstracts, 3814–3818.
- Hanafy, S. M., and G. T. Schuster, 2014, Interferometric interpolation of sparse marine data: *Geophysical Prospecting*, **62**, 1–16, doi: [10.1111/1365-2478.12066](https://doi.org/10.1111/1365-2478.12066).
- King, S., and A. Curtis, 2011, Velocity analysis using both reflections and refractions in seismic interferometry: *Geophysics*, **76**, no. 5, SA83–SA96, doi: [10.1190/geo2011-0008.1](https://doi.org/10.1190/geo2011-0008.1).
- Mallinson, I., P. Bharadwaj, G. T. Schuster, and H. Jakubowicz, 2011, Enhanced refractor imaging by super-virtual interferometry: *The Leading Edge*, **30**, 546–550, doi: [10.1190/1.3589113](https://doi.org/10.1190/1.3589113).
- Melo, G., and A. Malcolm, 2011, Microquake seismic interferometry with SVD-enhanced Green's function recovery: *The Leading Edge*, **30**, 556–562, doi: [10.1190/1.3589114](https://doi.org/10.1190/1.3589114).
- Melo, G., A. Malcolm, D. Mikesell, and K. van Wijk, 2010, Using SVD for improved interferometric Green's function recovery: 80th Annual International Meeting, SEG, Expanded Abstracts, 3986–3990.
- Mikesell, D., and K. van Wijk, 2011, Seismic refraction interferometry with a semblance analysis on the crosscorrelation gather: *Geophysics*, **76**, no. 5, SA77–SA82, doi: [10.1190/geo2011-0079.1](https://doi.org/10.1190/geo2011-0079.1).
- Mikesell, D., K. van Wijk, A. Calvert, and M. Haney, 2009, The virtual refraction: Useful spurious energy in seismic interferometry: *Geophysics*, **74**, no. 3, A13–A17, doi: [10.1190/1.3095659](https://doi.org/10.1190/1.3095659).
- Mooney, W. D., and C. S. Weaver, 1989, Regional crustal structure and tectonics of the Pacific coastal states: California, Oregon, and Washington: Chap. 9 of L. C. Pakiser, and W. D. Mooney, eds.: *Geophysical framework of the continental United States*: Geological Society of America memoir, **172**, 129–161.
- Musgrave, A. W., 1967, *Seismic refraction prospecting*: SEG.
- Nichols, J., D. Mikesell, and K. van Wijk, 2010, Application of the virtual refraction to near-surface characterization at the Boise hydrogeophysical research site: *Geophysical Prospecting*, **58**, 1011–1022, doi: [10.1111/j.1365-2478.2010.00881.x](https://doi.org/10.1111/j.1365-2478.2010.00881.x).
- Operto, S., and P. Charvis, 1996, Deep structure of the southern Kerguelen plateau (southern Indian Ocean) from ocean bottom seismometer wide-angle seismic data: *Journal of Geophysical Research*, **101**, 25077–25103, doi: [10.1029/96JB01758](https://doi.org/10.1029/96JB01758).

- Qin, F., Y. Luo, K. B. Olsen, W. Cai, and G. T. Schuster, 1992, Finite-difference solution of the eikonal equation along expanding wavefronts: *Geophysics*, **57**, 478–487, doi: [10.1190/1.1443263](https://doi.org/10.1190/1.1443263).
- Schuster, G. T., 2009, *Seismic interferometry*: Cambridge University Press.
- Shashkin, Y. A., 1991, *Fixed points*: American Mathematical Society.
- Sheriff, R. E., 2002, *Encyclopedic dictionary of applied geophysics*, 4th ed: SEG Publications.
- Snieder, R., and E. Safak, 2006, Extracting the building response using seismic interferometry: Theory and application to the Millikan Library in Pasadena, California: *Bulletin of the Seismological Society of America*, **96**, 586–598, doi: [10.1785/0120050109](https://doi.org/10.1785/0120050109).
- Snieder, R., K. van Wijk, M. Haney, and R. Calvert, 2008, The cancelation of spurious arrivals in Green's function extraction and the generalized optical theorem: *Physical Review E*, **78**, 317–326, doi: [10.1103/PhysRevE.78.036606](https://doi.org/10.1103/PhysRevE.78.036606).
- Snieder, R., K. Wapenaar, and K. Larner, 2006, Spurious multiples in seismic interferometry of primaries: *Geophysics*, **71**, no. 4, SI111–SI124, doi: [10.1190/1.2211507](https://doi.org/10.1190/1.2211507).
- Vasconcelos, I., and R. Snieder, 2008, Interferometry by deconvolution, Part 1 — Theory for acoustic waves and numerical examples: *Geophysics*, **73**, no. 3, S115–S128, doi: [10.1190/1.2904554](https://doi.org/10.1190/1.2904554).
- Wapenaar, K., and J. Fokkema, 2006, Green's function representations for seismic interferometry: *Geophysics*, **71**, no. 4, SI33–SI46, doi: [10.1190/1.2213955](https://doi.org/10.1190/1.2213955).
- Yu, J., and G. T. Schuster, 2004, Enhancing illumination coverage of VSP data by crosscorrelogram migration: 74th Annual International Meeting, SEG Expanded Abstracts, 2501–2504.

This article has been cited by:

1. Naveed Iqbal, Abdullatif A. Al-Shuhail, SanLinn I. Kaka, Entao Liu, Anupama Govinda Raj, James H. McClellan. 2017. Iterative interferometry-based method for picking microseismic events. *Journal of Applied Geophysics* **140**, 52-61. [[CrossRef](#)]
2. Shengpei An, Tianyue Hu, Gengxin Peng. 2017. Three-Dimensional Cumulant-Based Coherent Integration Method to Enhance First-Break Seismic Signals. *IEEE Transactions on Geoscience and Remote Sensing* **55**:4, 2089-2096. [[CrossRef](#)]
3. ShengPei An, TianYue Hu. 2016. Suppression of seismic surface waves based on adaptive weighted super-virtual interferometry. *Science China Earth Sciences* **59**:11, 2179-2188. [[CrossRef](#)]
4. Joachim Place, Alireza Malehmir. 2016. Using supervirtual first arrivals in controlled-source hardrock seismic imaging—well worth the effort. *Geophysical Journal International* **206**:1, 716-730. [[CrossRef](#)]
5. Sheng-Pei An, Tian-Yue Hu, Yong-Fu Cui, Wen-Sheng Duan, Geng-Xin Peng. 2015. Auto-pick first breaks with complex raypaths for undulate surface conditions. *Applied Geophysics* **12**:1, 93-100. [[CrossRef](#)]
6. Gerard T. Schuster. Seismic Interferometry Q1-1-Q1-41. [[Abstract](#)] [[References](#)] [[PDF](#)]